Available online at www.sciencedirect.com
ScienceDirect
Journal of Magnetic Resonance 183 (2006) 278–289
JMR Journal of Magnetic Resonance
www.elsevier.com/locate/jmr

Combined passive and active shimming for *in vivo* MR spectroscopy at high magnetic fields

Christoph Juchem [a,*], Bernd Muller-Bierl [b], Fritz Schick [b], Nikos K. Logothetis [a], Josef Pfeuffer [a,c]

[a] *Max-Planck Institute for Biological Cybernetics, Department of Physiology of Cognitive Processes, Spemannstrasse 38, 72076 Tübingen, Germany*
[b] *University of Tübingen, Section on Experimental Radiology, Hoppe-Seyler-Str. 3, 72076 Tübingen, Germany*
[c] *Siemens Medical Solutions, MR Applications Development, Karl-Schall-Strasse 6, 91052 Erlangen, Germany*

Received 13 June 2006; revised 1 September 2006
Available online 29 September 2006

Abstract

The use of high magnetic fields increases the sensitivity and spectral dispersion in magnetic resonance spectroscopy (MRS) of brain metabolites. Practical limitations arise, however, from susceptibility-induced field distortions, which are increased at higher magnetic field strengths. Solutions to this problem include optimized shimming, provided that active, i.e., electronic, shimming can operate over a sufficient range. To meet our shim requirements, which were an order of magnitude greater than the active shim capacity of our 7 T MR system, we developed a combined passive and active shim approach. Simple geometries of ferromagnetic shim elements were derived and numerically optimized to generate a complete set of second-order spherical harmonic shim functions in a modular manner. The major goals of the shim design were maximization of shim field accuracy and ease of practical implementation. The theoretically optimized ferro-shim geometries were mounted on a cylindrical surface and placed inside the magnet bore, surrounding the subject's head and the RF coil. *Passive* shimming generated very strong shim fields and eliminated the worst of the field distortions, after which the field was further optimized by flexible and highly accurate *active* shimming. Here, the passive-shimming procedure was first evaluated theoretically, then applied in phantom studies and subsequently validated for *in vivo* ^{1}H MRS in the macaque visual cortex. No artifacts due to the passive shim setup were observed; adjustments were reproducible between sessions. The modularity and the reduction to two pieces per shim term in this study is an important simplification that makes the method applicable also for passive shimming within single sessions. The feasibility of very strong, flexible and high-quality shimming via a combined approach of passive and active shimming is of great practical relevance for MR imaging and spectroscopy at high field strengths where shim power is limited or where shimming of specific anatomical regions inherently requires strong shim fields.

Keywords: Passive shimming; Active shimming; Field mapping; Ferromagnetism; Magnetic susceptibility

1. Introduction

Today's magnetic resonance spectroscopy (MRS) is not only used in analytical chemistry to retrieve detailed information about chemicals, but also for non-invasive *in vivo* experiments in biology and medicine to obtain quantitative information about biologically active compounds. Specifically, in the rapidly evolving field of neuroscience, MRS is of great importance, because it allows the assessment of neurochemical profiles of individual brain regions.

A non-homogeneous distribution of the magnetic field strength within the sensitive probe volume leads to broadening of spectral peaks and a reduction of the signal-to-noise ratio (SNR). Furthermore, the distribution of the magnetic field has a direct impact on the lineshape of spectral peaks, which may lead to quantification errors, if inappropriate model functions are used [1–3]. When magnetically susceptible probes are placed into the homogeneous field of an MR scanner, the field distribution often

* Corresponding author. Fax: +49 7071 601 652.
E-mail address: christoph.juchem@tuebingen.mpg.de (C. Juchem).

1090-7807/$ - see front matter © 2006 Elsevier Inc. All rights reserved.
doi:10.1016/j.jmr.2006.09.002

becomes inhomogeneous; a local distribution of field gradients is added. By correcting the field distribution accordingly, it can be made homogeneous with the probe inside the scanner ('shimming').

Shimming can be achieved by placing an ensemble of ferromagnetic objects with proper size and position into the magnetic field in order to improve the field homogeneity within the sensitive probe volume ('passive shimming') [4]. Passive shimming is not only used to improve the field homogeneity of the MR scanner [5–7], but also to compensate for field distortions induced by the subject [8–10]. However, a flexible shim method is required to account for varying conditions and passive shimming alone is not well suited to this task, because the physical mounting of many metal pieces is time consuming and inflexible. In practice, the utilisation of passive shimming has been mostly limited to special applications like the use of intra-oral passive shimming of the frontal cortex in humans via diamagnetic mouth inserts [11–13] or shimming the mouse brain by an optimized combination of paramagnetic and diamagnetic passive shims [14].

Magnetic fields, as vector fields, can be described by spherical harmonic functions. Accordingly, deviations from homogeneity can also be expressed on that basis. 'Active shimming' capitalizes on this principle, and by using a set of appropriate electrical coils, each generating a magnetic field component that corresponds to one spherical harmonic, minimizes field inhomogeneities by superimposing a shim field of the same magnitude but opposite sign to the distortion [4,15–17]. Iterative and analytical approaches have been proposed to optimize the active-shimming procedure for accuracy and speed. For *in vivo* conditions, it was demonstrated that the inclusion of second- and possibly third-order shim terms can considerably improve the field homogeneity and thereby the data quality for *in vivo* MR spectroscopy [18–20].

The first-order spherical harmonic terms X, Z, Y ($n = 1$, $m = 1, 0, -1$) and the second-order ones called $X2-Y2$, ZX, $Z2$, ZY, XY ($n = 2$, $m = 2, 1, 0, -1, -2$) are summarized in Table 1 in Cartesian coordinates and visualized in Fig. 1 for a unity sphere and a cylinder surface.

Table 1
Cartesian description of the z-components of the first- and second-order spherical harmonic shim fields

Abbreviation	Order (n)	Degree (m)	Function
X	1	1	x
Z	1	0	z
Y	1	−1	y
$X2-Y2$	2	2	$x^2 - y^2$
ZX	2	1	$z\,x$
$Z2$	2	0	$z^2 - (x^2 + y^2)/2$
ZY	2	−1	$z\,y$
XY	2	−2	$x\,y$

The fields are normalized to a uniform minimum-to-maximum range of −1 to 1 and visualized in Figs. 1a and b.

Shimming becomes of even greater importance in high-field scanners, which are being increasingly employed in both biomedical research and diagnostic medicine. The rationale for this trend is first based on the improved SNR, which is at least linearly related to the magnetic field strength for both MR imaging and spectroscopy [21]. Moreover, higher fields lead to better spectral dispersion in MR spectroscopy, which is of obvious advantage, when the task at hand is the separation of glutamate (Glu) and glutamine (Gln), or creatine (Cr) and phosphocreatine (PCr) in ^{1}H MRS of brain metabolites [22,23]. The benefit of better SNR and simplified spectra at high field strength can only be exploited if optimal shimming is achieved, as field distortions due to susceptibility effects also increase with field strength [22]. Increased field distortions require stronger shim fields, potentially exceeding the capabilities of the active shim device. In addition, regions of greatly differing magnetic susceptibilities, such as tissue–air transitions, e.g., in the vicinity of the ear canals or the cranial bone, may also require shim fields greater than those provided by active shimming. In practice, zero-order terms, i.e., field offsets, that are small compared to the scanner field strength, do not pose problems and first-order terms can be easily shimmed using the scanners' gradient system. Second-order terms, however, represent the main bottleneck in experimental setups when the shim requirements exceed the capabilities of the corresponding active shim device.

Here, we present a combined passive (ferromagnetic) and active (electronic) shimming approach for the generation of strong, high-accuracy second-order shim fields. Simple ferro-shim geometries were theoretically derived and optimized for maximum field strength and accuracy. Compared to earlier pure ferro-shim approaches [5–7,9,10] or a combination of passive and active shimming [9], the ease of implementation was a major design criterion. The placement of modular ferro-shim assemblies for the experimentally most relevant second-order shim terms in close proximity to the subject allowed the reproducible creation of shim fields many times larger than those of the scanner's built-in electronic shim device. Subsequently, active shimming with the scanner's shim device provided flexible fine tuning of the shim fields to the particular experimental conditions. The power of the combined passive- and active-shimming approach to improve the quality of brain MRS was demonstrated by shimming the macaque's visual cortex in a high-field 7 T MR scanner.

2. Methods

2.1. MR setup and subject

Measurements were performed on a 7 T/60 cm Bruker Biospec system (Bruker BioSpin, Ettlingen, Germany) [24,25] which was temporarily equipped with a Siemens gradient insert AC44 (40 mT/m, <200 μs, Siemens Medical Solutions, Erlangen/Germany). Anesthetized macaque

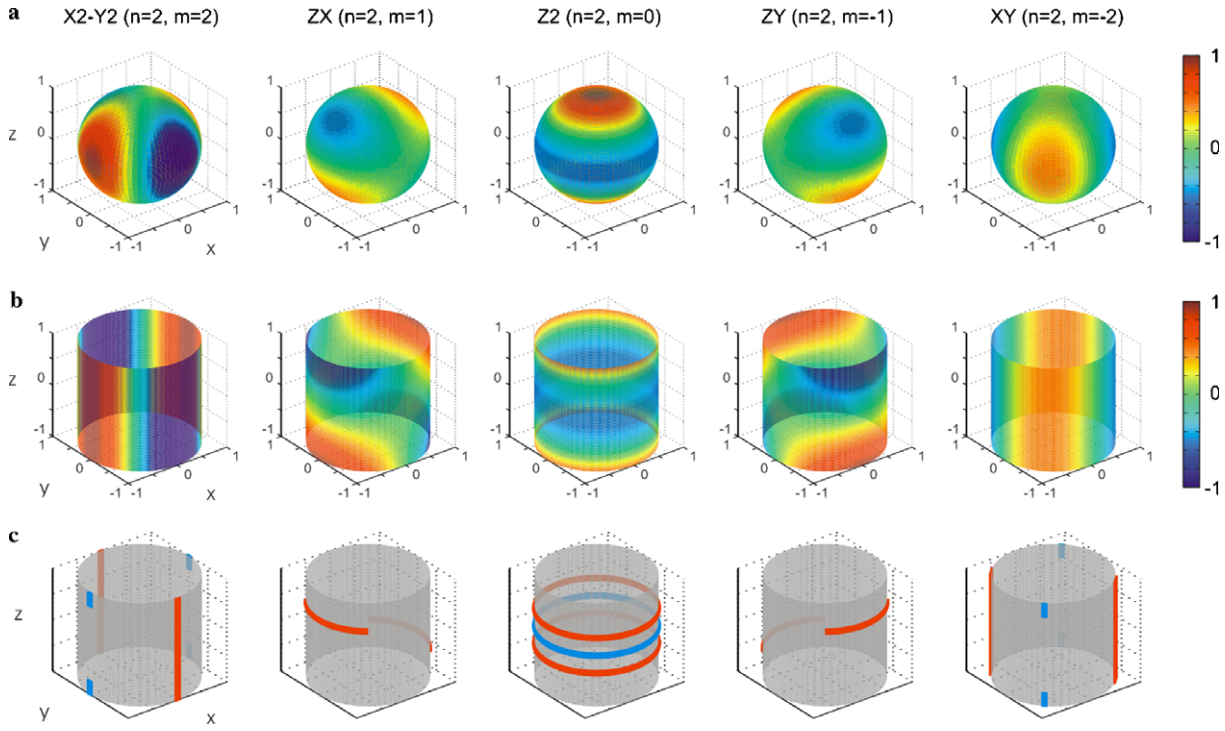

Fig. 1. 3D visualization of the second-order spherical harmonic functions $X2-Y2$, ZX, $Z2$, ZY, XY ($n=2$, $m=-2,-1,0,1,2$) for a sphere (a) and for a cylinder section (b). (c) Theoretical optimization of the ferro-shim design yields simple geometries of two pieces per shim term (red) for the generation of passive shim fields that approximate the corresponding spherical harmonics. The experimental effort for passive shimming with $+Z2$ and the amount of ferro-shim required for the $X2-Y2$, XY, and $+Z2$ terms could be minimized at tradeoffs in the shim field accuracy (blue). (For interpretation of the references to color in this figure legend, the reader is referred to the web version of this paper.)

monkeys (*Macaca mulatta*, $n=4$, 15 sessions total) were used and all procedures and experiments were approved by the local authorities and were in full compliance with the guidelines of the European Community (EUVD 86/609/EEC) for the care and use of laboratory animals. Surgical procedures, anesthesia, and details of the animal set-up were described previously [26]. A custom-made saddle coil (300 MHz) was used for spin excitation [25]. Signal acquisition for spectroscopy was done with an actively decoupled 35-mm surface coil (Bruker BioSpin, Ettlingen, Germany). Oblique geometry handling with respect to the laboratory coordinate system for MR imaging, shimming and spectroscopy was avoided by a 30–45° rotation of the monkey's head. The saddle coil was placed to the back of the monkey head and the surface coil was positioned over the visual cortex of one hemisphere. For single voxel spectroscopy, a STEAM sequence was used (FOV $5\times5\times5$ mm^3, TE 10 ms, TM 10 ms, TR 3 s) with VAPOR water suppression and outer volume suppression (OVS) as described in [27].

2.2. Field mapping

Magnetic fields were measured in two ways by using the saddle coil only: for full 3D field mapping, two FLASH images were acquired at different echo times of 7 and 9.5 ms (matrix $128\times128\times64$, FOV $64\times64\times64$ mm^3, TR 2 s) and the magnetic field distribution was calculated from the corresponding phase images. If necessary a 3D unwrapping [28] was applied, before the field distribution was fitted into first- and second-order spherical harmonic functions [29,30]. For the adjustment of the passive shimming, however, magnetic fields were mapped and analyzed using FASTMAP [18] on $10\times10\times10$ to $15\times15\times15$ mm^3 cube volumes.

2.3. Quality assessment of shim fields

A measure for the degree of similarity of the (theoretical or experimental) passive shim fields B^{passive} and the spherical harmonic target fields B^{harm} was needed for the quantitative evaluation of the accuracy of the passive shim fields. To this end, the classical Pearson product–moment correlation was modified as follows:

$$R^2 = 1 - \left(\frac{\sum_{i=1}^{n} B_i^{\text{passive}} B_i^{\text{harm}}}{\sqrt{\sum_{i=1}^{n} (B_i^{\text{passive}})^2 \sum_{i=1}^{n} (B_i^{\text{harm}})^2}} \right)^2 . \quad (1)$$

The magnetic field values B_i of all n spatial positions are equally weighted and the measure is invariant under global linear transformations, such as scalings and shifts. Due to the Cauchy–Schwarz inequality, the quotient is bounded in the range $[-1\ 1]$; the modified R^2 value is therefore zero for identical fields, approaching 1 as the field difference increases. By removing the subtraction of the means, it

provided a measure of the identity of two groups of point pairs, where relative offsets are considered as a decrease of similarity. The modified R^2 value, however, is a scalar and does not provide any information about the nature of contamination. In a second step of quality assessment the theoretically optimized shim fields were decomposed into first-to-fourth order spherical harmonic functions which provided a direct measure of the type and strength of residual deviations.

2.4. Magnetic properties of the permalloy used for passive shimming

For the generation of strong and reproducible passive shim fields at minimized mass requirements permalloy sheets were used (Ni–Fe alloy, VAC Vacuumschmelze, Hanau, Germany) due to the high-saturation magnetization and the minimum remanence and coercivity. The permalloy's saturation polarization was determined to be (0.752 ± 0.004) T with a superconducting quantum interference device (SQUID) magnetometer (Quantum Design MPMS-XL, San Diego/USA, 300 K, 0.3 T) at the Max-Planck Institute of Microstructure Physics in Halle, Germany. It was reached at approximately 0.4 T without coercivity (data not shown). The density of the metal alloy was measured as (8.611 ± 0.002) g/cm^3.

2.5. Theoretical design and optimization of passive shim fields

The goal of the geometrical design for passive shimming was to achieve both maximum accuracy and design simplicity. Based on dipole field theory and basic symmetry considerations, we chose ferro-shim geometries that would be most promising for the generation of the required fields. A cylinder geometry was selected as the basic design block in order to easily achieve rotational and planar symmetries. Calculations were used to validate and optimize the identity of the created shim fields and the spherical harmonic target functions. Given the magnetic susceptibility of the permalloy and the dimensions of the tube geometry, the expected shim fields were computed for different shim geometries when placed into a homogeneous magnetic field for which the saturation state of the magnetization was reached. The shim elements were discretized by a finite number of volume elements and a dipole field was attached to each volume element. The total field distortion was computed by superposition of the fields of the individual dipole fields. This ''dipole model'' has been shown to produce the correct field distribution at the limit of small volume elements [31,32]. The shim field distributions were calculated on a 3D data grid of size $101 \times 101 \times 101$ voxels. The ferro-shim geometries, by convention, were placed on the surface of an hypothetical cylinder with a diameter of 100 times the spacing of the point grid. Although spherical harmonics are dimensionless functions, shim fields have physical units. Since the spatial *pattern* of the passive shim fields was to be analyzed and optimized, rather than particular values, first the arbitrary scaling was removed. The integral of the root mean square differences within a 3D cube volume between the magnetic field and the spherical harmonic field was then determined and minimized. To this end, one optimized global linear transformation (i.e., a multiplication factor and an offset) was determined for the passive shim field. The numerical routine used for minimization was stopped when relative changes of both the scaling and the offset value dropped below 0.01%, which was always achieved in less than 10 iterations. The approach could be also understood as mimicking the physical process of shimming (mounting/unmounting of ferro-shim, frequency correction). Notably, the R^2 value was not used here as a target function for the determination of the optimal global linear transformation, since the measure was too sensitive and quickly approached 1 for considerably different field distributions. In contrast, the use of a conventional norm as the target function was numerically more stable. For evaluation and optimization of the permalloy geometries the centered $27 \times 27 \times 27$ grid points ($N = 19683$) of the full FOV were considered as the sensitive region for R^2 determination, which is 27%. Cubic spline interpolation was used to determine the optimum geometry condition for which R^2 was minimal. The robustness of the shim fields against non-optimal dimensioning of the shim geometries was determined as the range of the R^2 function around the optimum geometry, for which the R^2 values increased less than 0.01.

2.6. Experimental accomplishment of passive shimming

Thin pieces of maximally 10–12 mm length (e.g., $2 \times 0.5 \times 10$ mm^3) were concatenated with adhesive tape in a contact-free manner to assemble the derived larger structures, thereby minimizing the dimensions of conductive loops and the risk of generating eddy currents. For each shim term, a set of ferro-shim strips/blocks of different mass was prepared before the adjustment of a new shim tube was started. For the generation of a passive shim setup the field distribution of the region of interest was measured and the field inhomogeneities were decomposed into first- and second-order spherical harmonic functions. The required masses per shim term were calculated and an appropriate combination of layers was tightly fixed to the predefined positions on the surface of a plastic tube (length 34 cm, diameter 25 cm; Fig. 1c, in the following called 'shim tube'). The shim tube then was mounted on the monkey chair to surround the monkey head and the RF coils. It was positioned together with the subject inside the magnet bore and the gradient system. In order to modify the passive shimming for a first adjustment or later modifications, the animal chair was taken out of the magnet. The tube then was removed, modified and remounted onto the animal chair, and chair and monkey were brought back into the magnet.

2.7. Experimental validation of passive shim fields on a gel phantom

Based on the quantitative optimization results, the theoretically derived field patterns and strengths were experimentally controlled on an agar gel phantom. A $27 \times 27 \times 27\ mm^3$ FOV was used, corresponding to 11% of the 25 cm tube diameter. The passive shim field was determined from the condition of the mounted shim tube minus the field distribution without the shim tube which was fitted into first- and second-order spherical harmonics and removed by postprocessing. In some cases, experimental mounting asymmetries of the ferro-shims caused first-order shim terms, which were much smaller than the first-order shim capabilities of the gradient system. Here, we focused on the accuracy of the second-order shim terms, and since these were partially masked by the first-order contributions, the linear gradients were removed from the 3D field maps before the R^2 value determination.

2.8. Combined passive and active shimming in the monkey

The passive shim tube was adjusted once for a particular experimental setup, defined by the subject anatomy, target hemisphere, and head position. Field mapping with FASTMAP was used to quickly measure the field distortions in terms of the required shim fields. The subject was taken out of the magnet and modular ferro-shims were mounted on the shim tube based on the established requirements. In practice, it proved to be advantageous to start with the strongest requirements, before the others were added. This was because experimental misadjustments could not be avoided *per se*. For the adjustment of a new shim tube four to eight iterations (1–2 h) were required. Notably, the adjustment of a new shim tube required an almost complete removal of the field inhomogeneities by passive shimming to maximize the probability that the small dynamic range of active shimming was also sufficient for the following sessions.

3. Results

3.1. Theoretical generation of spherical harmonic shim functions by passive shimming

The $X2-Y2$ and XY shim fields were generated by pairs of ferro-shim lines placed vertically to the front and to the back of the shim tube or to opposite diagonal sides, respectively (Fig. 1c, red). The shape of the generated $X2-Y2$ and XY shim fields critically relied on the ratio of the length of the shim lines versus their distance given by the tube diameter with an optimum ratio of 1.205 ($R^2 = 0.01$). For a shim tube diameter of 25 cm, the optimal length of the vertical ferro-shim lines was 30.1 cm. For geometrical variations smaller than 0.065 (± 1.6 cm), the R^2 value increased by less than 0.01. Based on the saturation magnetization of the permalloy, the created shim field was calculated to be 0.054 Hz/(cm^2 g). Two quarters of a loop placed at the opposite sites of the shim tube were used to generate ZX/ZY shim terms (Fig. 1c). For a ratio of 0.359 for the vertical distance of the ring parts as compared to the tube diameter, a minimal R^2 value of 0.02 was found (9.0 cm for a tube diameter of 25 cm). The tolerances against the vertical displacement were determined to be 0.040 (± 1.0 cm) and the absolute ZX/ZY shim fields were calculated to be 2.50 Hz/(cm^2 g). For the four tesseral second-order shim fields, 90° rotations of the ferro-shim assemblies or a mirroring with respect to the center axial plane was enough to flip the polarity for the $X2-Y2/XY$ shims and the ZX/ZY shim terms, respectively. The zonal $Z2$ shim, however, required a qualitatively different shim constellation to achieve positive and negative polarity. In both cases, a parallel pair of loops was used, as proposed in [4], but separate optimizations of the ring distance versus the tube diameter were necessary to approximate the correct shape and polarity (Fig. 1c, red). For $+Z2$, a minimum R^2 value of 1×10^{-3} was achieved at a ratio of the ring distance versus the ring diameter of 0.236 (5.9 cm). The tolerance against misadjustment of the geometry ratio was determined to 0.045 and 0.026 at the low and the high ratio side, respectively (-1.1 cm/$+0.7$ cm). A minimum R^2 value as small as 1×10^{-4} was determined for $-Z2$ at a geometry ratio of 0.851 (21.3 cm). Shim strengths were determined as 2.11 and 1.38 Hz/(cm^2 g) for the $+Z2$ and $-Z2$ shim fields, respectively.

3.2. Tradeoffs for X2 − Y2/XY/+Z2 shimming

The ferro-shim mass that was needed to generate the $X2-Y2/XY$ fields of a given strength was many times higher than for the other exact shim terms. This was understandable, given the strong mutual cancellation effects that were necessary for the $X2-Y2/XY$ field profiling. Replacement of the two vertical ferro-shim lines by four blocks with vertical spacing at 90° intervals led to a field distribution that was a combination of $X2-Y2/XY$ and $-Z2$ shim fields (Fig. 1c, blue). Due to the vertical gaps between the blocks the mutual cancellation effects were greatly reduced and the amount of ferro-shim that was necessary to generate the same strength of the $X2-Y2/XY$ shim field was 4.9 times smaller than that of the two line element approach. A minimal R^2 value of 0.01 was found for a ratio of 1.009 (25.2 cm) for the vertical block distance versus the tube diameter and a reasonable tolerance limit could be determined only at the low ratio side (0.165/4.1 cm) because R^2 values remained small for larger vertical distances of the ferro-shim blocks. For the $+Z2$ shim term, the double loop structure was reduced and simplified to a single loop centered horizontally around the iso-center. The generated field distribution matched the theoretical target function, but the overall accuracy of the generated shim field was reduced relative to the two-loop approach.

The results of difference calculations between the attained passive shim fields and the spherical harmonic target fields are depicted in Fig. 2.

3.3. Theoretical field-of-view dependence of the passive shimming

The optimization of the theoretical ferro-shim geometries included an FOV that was 27% of the shim tube diameter. An analysis of the shim field accuracy as a function of the FOV size was done to determine (for the optimization result at 27% FOV) the maximum FOV for which the spherical harmonic target fields were sufficiently well approximated. Notably, the $-Z2$ contribution was removed from the block design field distributions $X2-Y2/XY$ before the R^2 value calculation. Shim fields almost perfectly approximated the spherical harmonic target functions for small FOV size, and the reduction of the shim field accuracy was moderate for voxel sizes up to 40–50% of the shim tube diameter (Fig. 3) (see Table 2).

3.4. Theoretical analysis of residual field contamination

The deviations of the theoretically computed shim fields from the spherical harmonic target fields were analyzed by fitting the passive shim fields to the first-to-fourth order

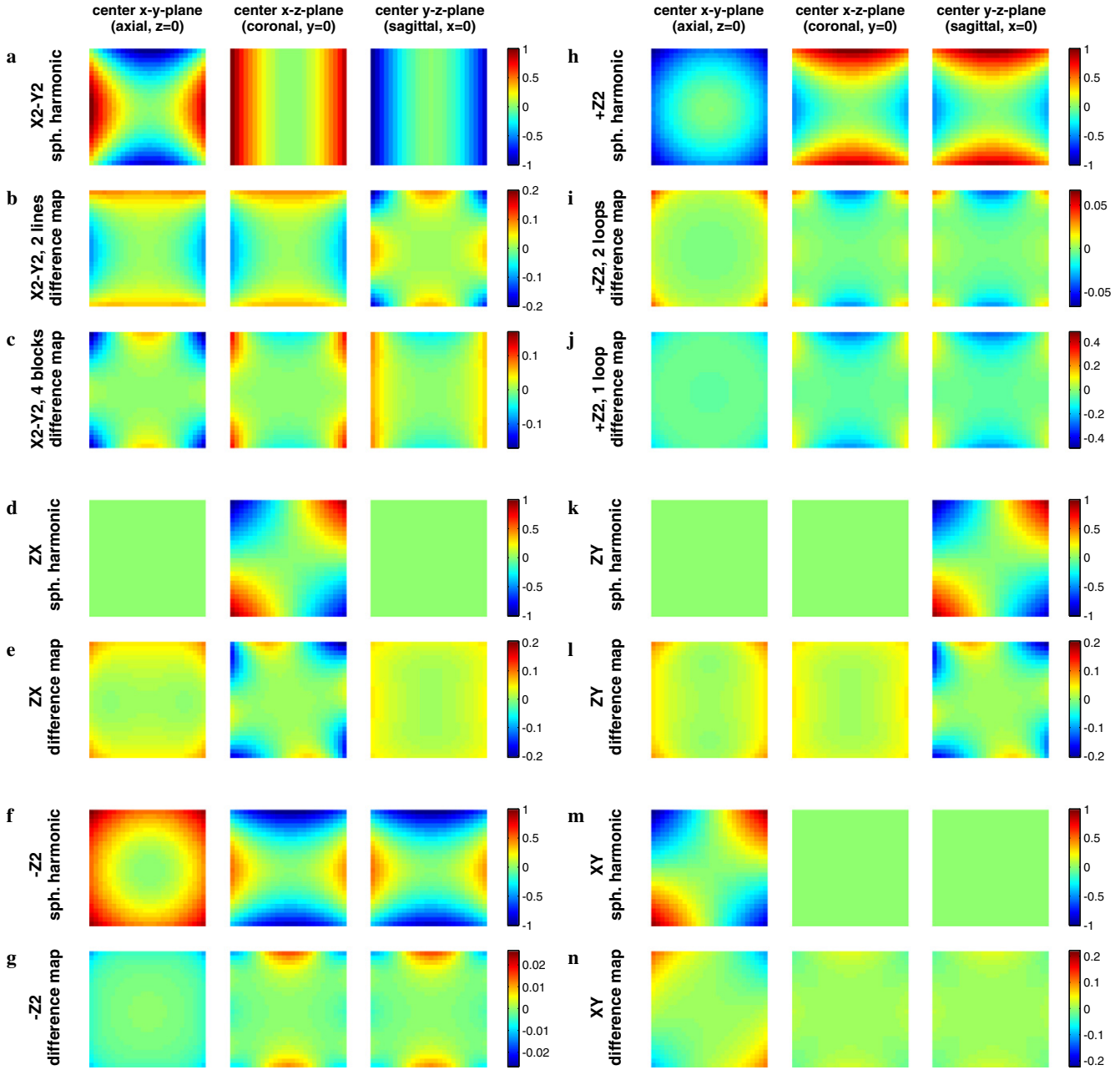

Fig. 2. Quality assessment of the theoretically optimized passive shim fields. The three center slices are shown for each of the second-order spherical harmonic target fields (a, d, f, h, k, and m) and followed by difference images of the attained passive shim fields minus the target fields (in [a.u.]). In (c) the $-Z2$ contamination of the four block shim design for $X2-Y2$ was removed before the difference analysis.

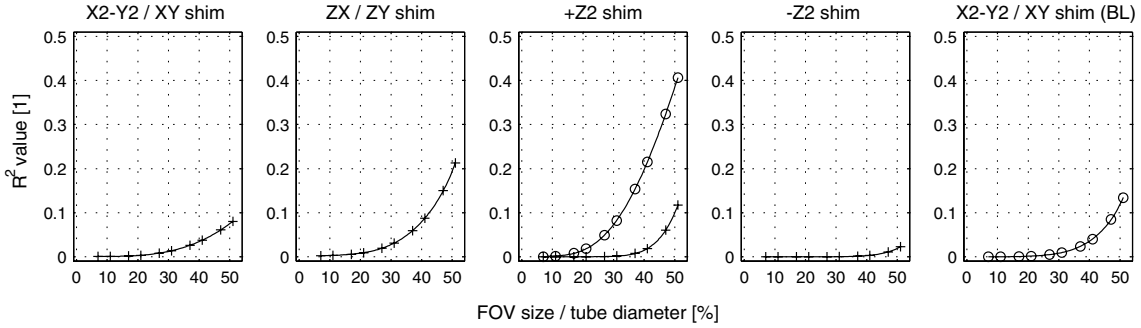

Fig. 3. Comparison of the theoretically optimized passive shim fields to the second-order spherical harmonic target fields as a function of the FOV size. The optimization results for FOVs of 27% of the tube diameter were analyzed for the two pieces approach (Fig. 1c, red; symbol: '+') as well as for the four block shim tradeoffs (BL) for $X2-Y2/XY$ and the single loop solution for $+Z2$ (Fig. 1c, blue; symbol: 'o'). The passive shim fields closely approximated the target fields for reasonably small FOVs.

Table 2
Ferro-shim optimization results for the generation of the second-order spherical harmonic shim functions

Passive shim field	$X2-Y2/XY$	ZX/ZY	$+Z2$ (double)	$-Z2$	$X2-Y2/XY$ (BL)	$+Z2$ (single)
R^2_{opt}	0.01	0.02	0.001	0.0001	0.01	0.05
Optimized ratio [1]	1.205	0.359	0.236	0.851	1.009	—
Optimized ratio (cm)	30.1	9.0	5.9	21.3	25.2	—
Theo. field/mass [Hz/(cm^2 g)]	0.054	2.50	2.11	1.38	0.27	4.94
Exp. field/mass [Hz/(cm^2 g)]	0.056 (0.001)	2.36 (0.12)	1.98 (0.02)	1.26 (0.01)	0.27 (0.01)	4.61 (0.06)

Minimum R^2 values <0.02 were achieved for all fields, indicating a high degree of similarity between the passive shim fields and the corresponding spherical harmonics. Based on the saturation magnetization of the permalloy used for passive shimming, quantitative field strengths were deduced theoretically and proven in phantom experiments (mean (std.)).

spherical harmonics. Because all shim geometries were chosen to be symmetrical with respect to the three main axes, first-order terms, i.e., linear field gradients, were not observed. The attained second-order field contributions are shown in Table 3. They were normalized with respect to the appropriate field term to evaluate the proportion of desired versus non-desired field contributions. For all except one of the passive shim fields, the field terms to be generated exceeded the unwanted ones by at least a factor of 10. The only exception was the $X2-Y2$ tradeoff shim achieved with 4 blocks of ferro-shim, for which the $-Z2$ contamination was three times larger than the desired field term. Because strong and accurate $+Z2$ shim fields were easy to accomplish, the drawback for the generation of strong $X2-Y2/XY$ shim fields was of only minor importance. In all cases, third-order contributions were negligible and values of the fourth-order field contributions ([Hz/cm^4]) did not exceed $\pm 1\%$ of the generated second-order shim fields ([Hz/cm^2]).

3.5. Experimental validation of passive shim fields on a gel phantom

Phantom field mapping confirmed the theoretical optimization results of all shim fields and polarities. Modified R^2 values below 0.02 were achieved in all cases, and

Table 3
Spherical harmonics decomposition of the theoretically optimized second-order shim field distributions (normalized for the desired field term)

	$X2-Y2$	ZX	$Z2$	ZY	XY
$X2-Y2$	1	0	0.05	0	0
$X2-Y2$ (BL)	1	0	−2.99	0	0
ZX	−0.05	1	−0.05	0	0
$Z2$ (single)	0	0	1	0	0
$Z2$ (double)	0	0	1	0	0
$-Z2$	0	0	1	0	0
ZY	0.05	0	−0.05	1	0
XY	0	0	0.01	0	1

For all except one of the passive shim fields, the desired field terms exceeded the unwanted ones by at least a factor of 10. The only exception was the four block (BL) tradeoff design for $X2-Y2/XY$ shimming for which the concomitant $-Z2$ contamination was found to be three times larger than the desired one. The 4.9-fold enhancement in field strength and the ease of strong and accurate $+Z2$ shimming, however, made the four block approach a reasonable experimental tradeoff.

deviations from the target field distributions were small (Fig. 4). Consistent with the theoretical predictions, first-to-fourth order fitting confirmed that artifactual third- and fourth-order terms were not generated.

3.6. Shimming for ^1H MR spectroscopy of the macaque visual cortex at 7 T

The improvement of the achievable magnetic field homogeneity by combined passive and active shimming of the macaque monkey brain *in vivo* was addressed by quantitative field mapping (Fig. 5).

The yellow box assigns the $10 \times 10 \times 10\ mm^3$ ROI placed onto the visual cortex gray and white matter. The field distributions after active shimming only (given the current hardware constraints), and after shimming with the combined passive and active approach, were compared. A 3D field map was acquired at zero shim before the different types of shimming were applied, to quantify the distortions of the magnetic field and thus the shim fields required to correct for them. Decomposition of the ROI's field distribution into spherical harmonics revealed second-order terms of $X2-Y2$, 3.9 Hz/cm^2; ZX, −19.0 Hz/cm^2; $Z2$, −75.0 Hz/cm^2; ZY, 33.6 Hz/cm^2; XY, −3.3 Hz/cm^2. First- and second-order field decomposition of at least five field maps per shim channel in a previous phantom study provided the full correlation matrix of the currently installed AC44 shimming device. Linear regression of the data points yielded maximum shim field strengths of $X = 589$ Hz/cm, $Z = 587$ Hz/cm, and $Y = 511$ Hz/cm for the linear shim terms and $X2-Y2 = 1.86$ Hz/cm^2, $ZX = 3.74$ Hz/cm^2, $Z2 = 5.21$ Hz/cm^2, $ZY = 3.69$ Hz/cm^2, $XY = 1.84$ Hz/cm^2 for the second-order ones at correlation coefficients >0.98 in all cases. Considering the interdependencies of the shim channels for all eight first- and second-order terms, the absolute field distortions translated to relative shim field requirements of $X2-Y2$, 365%; ZX, −465%; $Z2$, 1540%; ZY, −970%; XY, −130% with respect to the currently available active shim power. After constrained active shimming only large-scale field fluctuations remained in the brain (Fig. 5a). Simple mounting of the shim tube, which had been adjusted in a previous session 6 weeks before, was enough to remove the main field inhomogeneities and to permit optimal first- and second-order active shimming. Although the shimming was focused on improving the homogeneity within the localized $10 \times 10 \times 10\ mm^3$ cube volume inside the brain, the major large-scale field fluctuations were considerably reduced (Fig. 5b). Strong frequency variations with a range of 100 Hz remained within the ROI after constrained active shimming, whereas the frequency spread was reduced by a factor of 2 in this case with combined passive and active

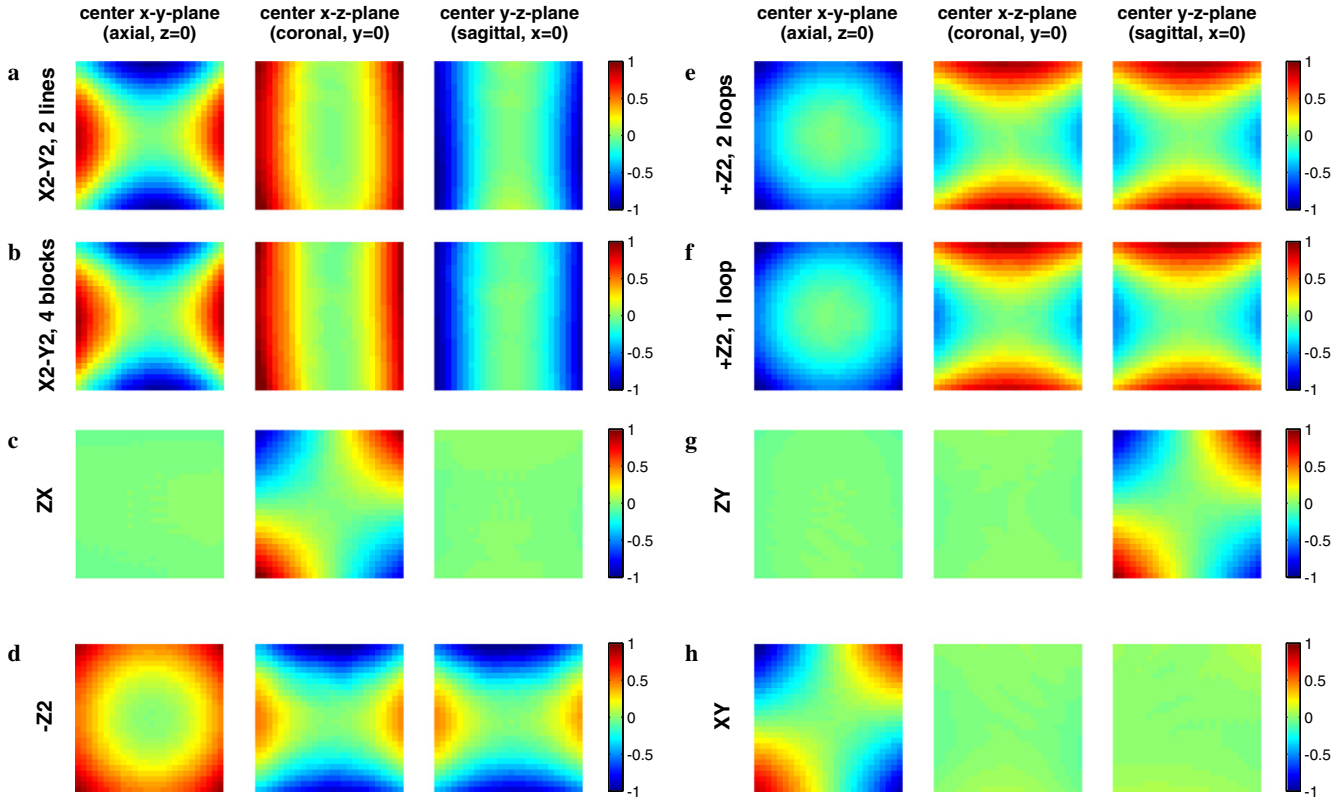

Fig. 4. Experimental validation of the generation of the second-order passive shim fields on a gel phantom. A gradient echo FLASH imaging sequence with an isotropic resolution of 1 mm at 7/9.5 ms echo time was used to measure the field distributions from a $27 \times 27 \times 27\ mm^3$ cube voxel (11% FOV, shim tube diameter 25 cm, in [a.u.]). The second-order spherical harmonics were well approximated by the passive shimming and $R^2 < 0.02$ was achieved in all cases.

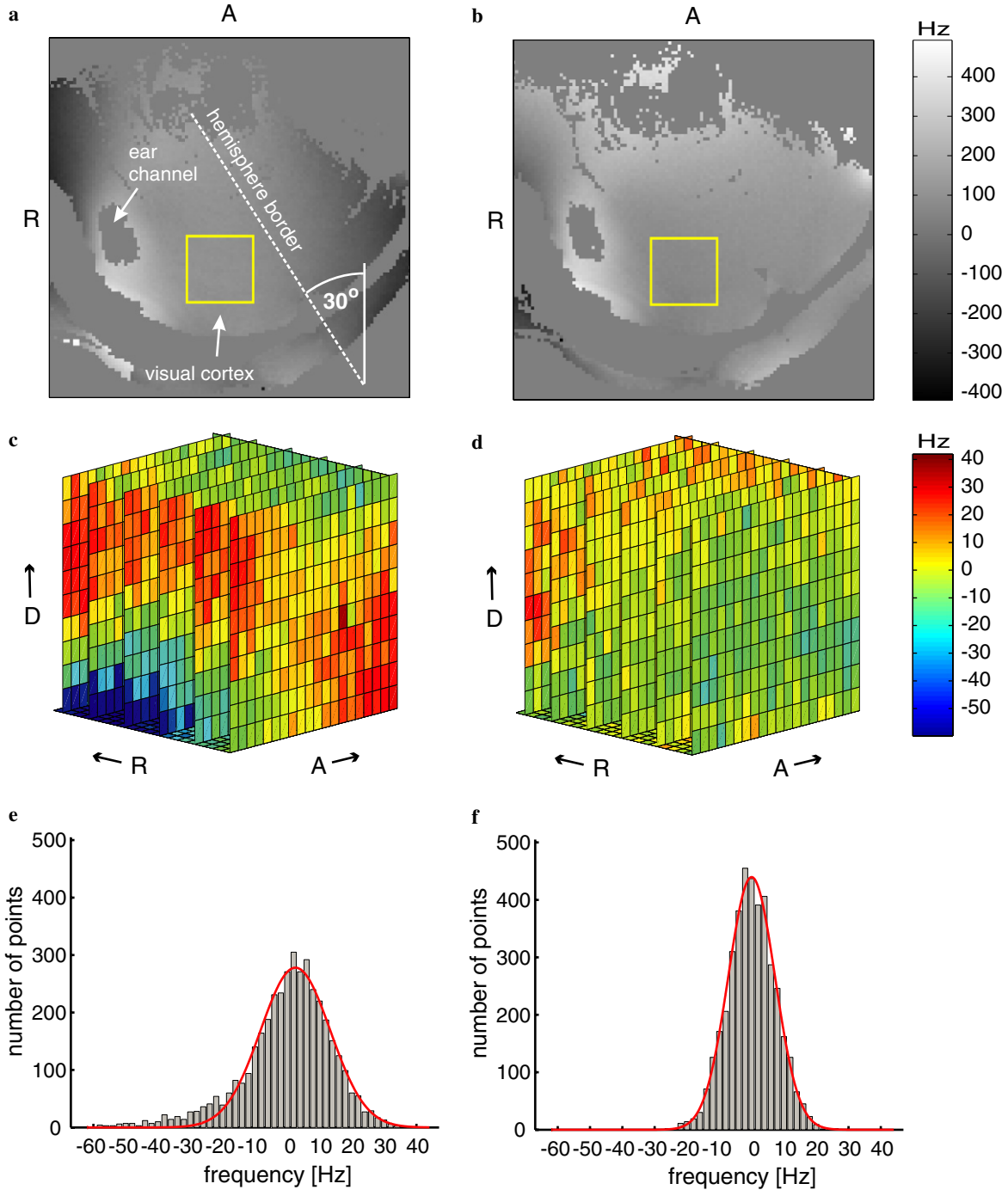

Fig. 5. Comparison of the combined passive and active shimming with constrained active shimming only for field homogenization of the visual cortex of a macaque monkey at 7 T. Axial field maps from the 30° rotated monkey head of the constrained (a) and of the combined (b) shimming are depicted (A, anterior; R, right; D, dorsal). The shimming volume, placed into the visual cortex gray and white matter, is indicated by the yellow box. Field deviations of several hundred Hertz remained over the brain after active shimming only (a), whereas the major large-scale field distortions were removed by the combined shimming (b). Maximum frequency differences were about 100 Hz in the purely actively shimmed voxel (c) and reduced by a factor of 2 after combined shimming (d). The FWHM of the Gaussian fitted frequency distribution was reduced from 25.4 to 17.0 Hz (e,f). (For interpretation of the references to color in this figure legend, the reader is referred to the web version of this paper.)

shimming (Figs. 5c and d). The full width at half maximum (FWHM) of the Gaussian fitted frequency distribution was reduced from 25.4 to 17.0 Hz.

With the combination of passive and active shimming, linewidths of 11–13 Hz for water and 9.5–12 Hz for the Cr + PCr resonance at 3 ppm were reproducibly achieved in $5 \times 5 \times 5$ mm^3 (125 μL) MRS voxels from the visual cortices of different monkeys and hemispheres. No additional artifacts such as B_0 eddy currents or spikes were observed in any of the MR spectroscopy (or imaging) data that

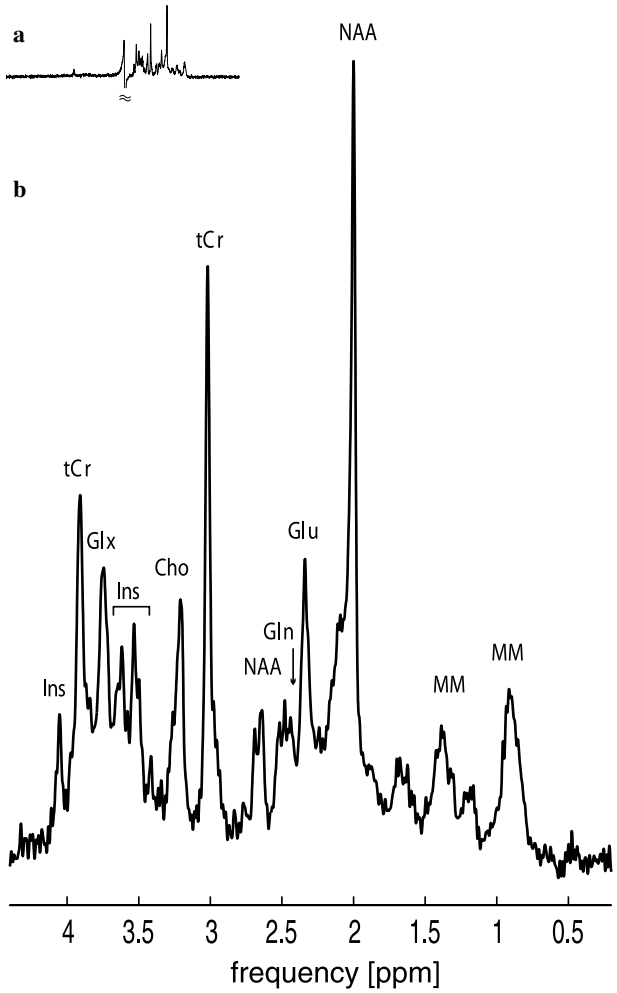

Fig. 6. ^{1}H MR spectrum from the visual cortex of a macaque monkey at 7 T (STEAM, NA 1024/51 min). A modest exponential line-broadening of 1 Hz was applied before Fourier transformation and zero-order phasing. First-order phasing was not necessary, and the baseline was flat outside the spectral regions of metabolites and water without correction (a). Linewidths were measured to 11.0 Hz for water and 9.6 Hz for the creatine + phosphocreatine (Cr + PCr) methyl singlet at 3 ppm. The spectral quality and SNR were sufficient to quantify more than 10 metabolites.

could be attributed to passive shimming. Neither baseline correction nor first-order phasing was required in any of the experiments. In the presented spectrum more than 10 metabolites could be quantified from a voxel of visual cortex gray and white matter (Fig. 6). Notably, γ-aminobutyric acid (GABA) was above the detection limit as defined by a 20% threshold of the Cramér–Rao Lower Bounds (CRLB) glutamate could be separated from glutamine, and creatine from phosphocreatine.

4. Discussion

Here we report a combined passive–active shimming methodology that can be used to achieve excellent homogeneity in high-field scanners. High-resolution MRS greatly benefits from high fields, but at the same time the detrimental effects of field inhomogeneities, such as susceptibility-induced field distortions, increase with field strength.

Often, the electronic shimming may be of insufficient power to permit homogenization at the desired spatial scale. To meet our shim requirements, which were an order of magnitude greater than the shim capacity of our 7 T system, we developed a combined passive and active shim approach.

Simple ferro-shim geometries were derived to generate field distributions very similar to the second-order spherical harmonic functions. The theoretically optimized shim fields were experimentally validated *in vitro* on a gel phantom as well as *in vivo* in the monkey brain. Experimental frequency shifts caused by offsets inherent to the passive shimming and experimental imperfections accumulated up to ±3 kHz. However, compared to the Larmor frequency of 300 MHz, at 7 T these field drifts were considered to be negligible with respect to potential effects on the signal strength and dispersion of the ^{1}H brain metabolite spectra.

The measurement of the saturation magnetization of the permalloy allowed the calculation of absolute passive shim fields and enabled a direct comparison of theoretical optimizations and experimental results. The magnetization curve of the ferromagnetic permalloy was saturated at an external magnetic field strength of 0.4 T. Consequently, there was no risk of memory effects in our 7 T MR system for repetitive use of the ferro-shims and the absolute shim fields generated by a particular shim tube could be expected to remain unchanged. The results are valid not only for the particular metal alloy and magnetic field strength used in this study, but for all magnetic field strengths and ferromagnetic materials for which the saturation state is certainly reached. Rescaling the shim fields by the ratio of the saturation magnetizations provides a direct guide for the generation of second-order shim terms and absolute strengths in other setups.

The size of the monkey head is approximately 50% of the human head in a linear dimension; spatial regions to be shimmed (for example for single voxel MRS) are scaled down accordingly. The optimization analysis of a 27% FOV (6.8 cm for the tube diameter of 25 cm) was reasonable and sufficient for the monkey setup, since this FOV size covered a large part of the brain. The passive-shimming method can be applied to the human setup simply by scaling up the tube diameter and all shim dimensions by a factor of 2–3. Because tolerances against experimental variations scale accordingly, relative errors will be even smaller than those in the monkey setup.

A Siemens gradient/shim insert AC44, originally designed for human head scanners operating at a 3 T field, was used for active shimming. Therefore, the active shim capabilities were not expected to meet the requirements for shimming the brain of the macaque monkey at 7 T. In fact, the available capabilities were regularly exceeded for all second-order channels multiple times and were always highest for the $Z2$ term with values of 800–1500% of the available shim power. This finding of strong $-Z2$

field distortions qualitatively fits with data from the human brain at 3 T [30]. For all monkeys, the shim requirements were qualitatively comparable between equal setups, but the absolute values varied up to a factor of 2, with the example presented in Fig. 5 posing the highest requirements. Strong $X2-Y2/XY$ shim field distortions favored the tradeoff approach of four blocks of ferro-shim (instead of four lines) for experimental purposes. The generation of strong and accurate $+Z2$ shim fields to compensate for the induced $-Z2$ terms was easy to achieve and the four blocks approach furthermore permitted the independent mounting and unmounting of all shim terms and avoided geometrical crossings. For $Z2$ shimming, both the ease of mounting a single loop and the 2.4-fold enhancement of the shim field at identical ferro-shim mass, made this approach preferable for our geometrical conditions. With the tradeoffs for $X2-Y2/XY$ and $+Z2$ shimming, the total mass requirements for the shim tubes were below 70 g and were mainly dominated by the $X2-Y2/XY$ terms, since these still provided the lowest field strength per ferro-shim mass. High reproducibility of the setup and of the positioning of the monkey head and the shim tube was considered a key point for reproducible shimming conditions. As determined by MR imaging, spatial deviations of the brain position were in the range of 0–2 mm between sessions and rotations were negligible. Moderate reproducibility of other setups (like clinical scanners) might be a limiting factor for the repetitive use of a fixed ferro-shim geometry for passive shimming. Minimum experimental effort was required to implement the simple ferro-shim geometries of only two (multi-layer) pieces per shim term. The ease of implementation suggests that the combination of active and modular passive shimming might be a reasonable way to overcome insufficient shim power even in less reproducible setups, where modifications in each session are required. Furthermore, MR imaging and spectroscopy in rodents, for which setups are also well defined and inter-subject variations of the anatomy and the shim requirements are limited, could use passive shimming based on a default shim tube for a pre-shim adjustment. This method of combined modular passive and active shimming is of high practical relevance in particular for high field MR setups and/or shimming of regions which inherently require high second-order shim fields, like the skull region, the vicinity of the ear canals or the orbitofrontal cortex.

In this paper, we present a means of generating the five second-order spherical harmonic shim fields by modular passive shimming. In addition, we propose reasonable experimental tradeoffs for $+Z2$ shimming (single loop elements) and $X2-Y2/XY$ shimming (four block elements). A cylindrical geometry was used as the basic design module to achieve the simplest ferro-shim geometries for minimal ferro-shim mass. The basic design module for the generation of shim fields by passive shimming used in [4] was a sphere. The transformation of the numerically optimized ratios for $\pm Z2$ shimming ($+Z2$, 0.24; $-Z2$, 0.85) into angles yield values of 76.7° and 49.6° which nicely reproduced the analytical results of 76.2° and 48.6°, respectively. This cross-check of methods further validates the numerical analysis developed and the optimization procedure presented in this study. The advantage of the numerical method used here is that it allows the direct analysis of the quality of field distributions for particular, even complex, geometrical conditions. For the ZX/ZY shim terms we used two quarters of a loop to generate reasonable shim fields and two line elements or four blocks for the $X2-Y2/XY$ shims. In Ref. [4] at least 11 pieces were necessary for the generation of ZX/ZY shim terms and no less than 17 pieces for $X2-Y2/XY$ shimming. Elegant and more general solutions for passive shimming with ferromagnetic material have been proposed which might additionally include higher-order terms. The drawback of these techniques, however, is that they require many hundreds or even more than 1000 metal pieces [9,10]. The modularity and the reduction to two pieces per shim term in this study is an important simplification of passive shimming that makes the method applicable also for passive shimming within single sessions. Because we started from dipole theory and basic symmetry considerations with somewhat arbitrary default geometries, we do not claim that the proposed design for passive shimming is the best solution possible for accuracy of shim fields and ease of experimental implementation. On the basis of symmetry, however, we consider it unlikely that solutions with less than two pieces of ferro-shim for $X2-Y2$, XY, ZX, ZY and $-Z2$ can be found.

Acknowledgments

The authors thank Dr. Kornelius Nielsch and Dr. Mihaela Daub (Max-Planck Institute for Microstructure Physics, Halle, Germany) for the measurement of the magnetization curve of the permalloy, Dr. Rhodri Cusack (MRC Cognition and Brain Science Unit, Cambridge/England) for providing the 3D phase unwrapping algorithm, available on his website, and Dr. Hellmut Merkle (National Institute of Health, Bethesda/USA), Dr. Sascha Juchem (Frankfurt/Germany) and Dr. Hansjörg Graf (University of Tübingen, Tübingen/Germany) for helpful discussions. This work was supported by the Max-Planck Society.

References

[1] L. Vanhamme, T. Sundin, P.V. Hecke, S.V. Huffel, MR spectroscopy quantitation: a review of time-domain methods, NMR Biomed. 14 (2001) 233–246.
[2] S. Mierisova, M. Ala-Korpela, MR spectroscopy quantitation: a review of frequency domain methods, NMR Biomed. 14 (2001) 247–259.
[3] R. Stoyanova, T.R. Brown, NMR spectral quantitation by principal component analysis, NMR Biomed. 14 (2001) 271–277.
[4] F. Romeo, D.I. Hoult, Magnet field profiling: analysis and correcting coil design, Magn. Reson. Med. 1 (1984) 44–65.
[5] J.V.M. McGinley, V.C. Srivastava, G.D. DeMeester, Passive Shimming Technique for MRI Magnets, US patent 5,532,597, 1996.

[6] B. Dorri, Method for Passively Shimming a Magnet, US patent 5,677,854, 1997.
[7] G. Neuberth, Integral Passive Shim System for a Magnetic Resonance Apparatus, US patent 6,897,750 B2, 2005.
[8] A. Jesmanowicz, V. Roopchansingh, R.W. Cox, P. Starewicz, W.F.B. Punchard, J.S. Hyde, Local Ferroshims Using Office Copier Toner. ISMRM, annual meeting 2001, Glasgow/Scotland.
[9] A. Jesmanowicz, J.S. Hyde, W.F.B. Punchard, P.M. Starewicz, Method for Shimming a Static Magnetic Field in a Local MRI Coil, US patent 6,294,972 B1, 2001.
[10] D.F. Hillenbrand, K.M. Lo, W.F.B. Punchard, T.G. Reese, P.M. Starewicz, High-order MR shimming: a simulation study of the effectiveness of competing methods, using an established susceptibility model of the human head, Appl. Magn. Reson. 29 (2005) 39–64.
[11] J.L. Wilson, M. Jenkinson, P. Jezzard, Optimization of static field homogeneity in human brain using diamagnetic passive shims, Magn. Reson. Med. 48 (2002) 906–914.
[12] J.L. Wilson, P. Jezzard, Utilization of an intra-oral diamagnetic passive shim in functional MRI of the inferior frontal cortex, Magn. Reson. Med. 50 (2003) 1089–1094.
[13] R. Cusack, B. Russell, S.M. Cox, C. De Panfilis, C. Schwarzbauer, R. Ansorge, An evaluation of the use of passive shimming to improve frontal sensitivity in fMRI, Neuroimage 24 (2005) 82–91.
[14] K.M. Koch, P.M. Brown, D.L. Rothman, R.A. De Graaf, Adjustable Subject-Specific Passive Shims using Optimized Distributions of Bismuth and Zirconium. ISMRM, annual meeting 2006, Seattle/USA.
[15] P. Konzbul, K. Sveda, Shim coils for NMR and MRI solenoid magnets, Meas. Sci. Technol. 6 (1995) 1116–1123.
[16] M.A. Brideson, L.K. Forbes, S. Crozier, Determining complicated winding patterns for shim coils using stream functions and the target-field method, Concepts Magn. Reson. 14 (2001) 9–18.
[17] M.A. Brideson, L.K. Forbes, S. Crozier, Winding patterns for actively shielded shim coils with asymmetric target-fields, Meas. Sci. Technol. 14 (2003) 484–493.
[18] R. Gruetter, C. Boesch, Fast, noniterative shimming of spatially localized signals. *In vivo* analysis of the magnetic field along axes, J. Magn. Reson. 96 (1992) 323–334.
[19] D.M. Spielman, E. Adalsteinsson, K.O. Lim, Quantitative assessment of improved homogeneity using higher-order shims for spectroscopic imaging of the brain, Magn. Reson. Med. 40 (1998) 376–382.
[20] Z. Chen, S.S. Li, J. Yang, D. Letizia, J. Shen, Measurement and automatic correction of high-order B0 inhomogeneity in the rat brain at 11.7 Tesla, Magn. Reson. Imaging 22 (2004) 835–842.
[21] K. Ugurbil, G. Adriany, P. Andersen, W. Chen, M. Garwood, R. Gruetter, P.G. Henry, S.G. Kim, H. Lieu, I. Tkac, T. Vaughan, P.F. Van De Moortele, E. Yacoub, X.H. Zhu, Ultrahigh field magnetic resonance imaging and spectroscopy, Magn. Reson. Imaging 21 (2003) 1263–1281.
[22] R. Gruetter, S.A. Weisdorf, V. Rajanayagan, M. Terpstra, H. Merkle, C.L. Truwit, M. Garwood, S.L. Nyberg, K. Ugurbil, Resolution improvements in in vivo 1H NMR spectra with increased magnetic field strength, J. Magn. Reson. 135 (1998) 260–264.
[23] I. Tkac, P. Andersen, G. Adriany, H. Merkle, K. Ugurbil, R. Gruetter, In vivo 1H NMR spectroscopy of the human brain at 7 T, Magn. Reson. Med. 46 (2001) 451–456.
[24] C. Juchem, H. Merkle, F. Schick, N.K. Logothetis, J. Pfeuffer, Region and volume dependencies in spectral line width assessed by (1)H 2D MR chemical shift imaging in the monkey brain at 7 T, Magn. Reson. Imaging 22 (2004) 1373–1383.
[25] J. Pfeuffer, H. Merkle, M. Beyerlein, T. Steudel, N.K. Logothetis, Anatomical and functional MR imaging in the macaque monkey using a vertical large-bore 7 Tesla setup, Magn. Reson. Imaging 22 (2004) 1343–1359.
[26] N.K. Logothetis, H. Guggenberger, S. Peled, J. Pauls, Functional imaging of the monkey brain, Nat. Neurosci. 2 (1999) 555–562.
[27] J. Pfeuffer, C. Juchem, H. Merkle, A. Nauerth, N.K. Logothetis, High-field localized (1)H NMR spectroscopy in the anesthetized and in the awake monkey, Magn. Reson. Imaging 22 (2004) 1361–1372.
[28] R. Cusack, N. Papadakis, New robust 3-D phase unwrapping algorithms: application to magnetic field mapping and undistorting echoplanar images, Neuroimage 16 (2002) 754–764.
[29] H. Wen, F.A. Jaffer, An in vivo automated shimming method taking into account shim current constraints, Magn. Reson. Med. 34 (1995) 898–904.
[30] S. Clare, J. Evans, P. Jezzard, Requirements for room temperature shimming of the human brain, Magn. Reson. Med. 55 (2005) 210–214.
[31] B. Muller-Bierl, H. Graf, U. Lauer, G. Steidle, F. Schick, Numerical modeling of needle tip artifacts in MR gradient echo imaging, Med. Phys. 31 (2004) 579–587.
[32] B. Muller-Bierl, H. Graf, G. Steidle, F. Schick, Compensation of magnetic field distortions from paramagnetic instruments by added diamagnetic material: measurements and numerical simulations, Med. Phys. 32 (2005) 76–84.